Document Title:	**LIBS for Soil Screening Study of Matrix Effects on Elemental Profiling**
Author(s):	**Matthieu Baudelet, Ph.D.**
Document Number:	**252776**
Date Received:	**March 2019**
Award Number:	**2013-DN-BX-K006**

Agency: NATIONAL INSTITUTE OF JUSTICE

Grant Number: 2013-DN-BX-K006

Project title: NIJ Award Detail: LIBS for Soil Screening Study of Matrix Effects on Elemental Profiling

PI: Dr. Matthieu Baudelet

Submission date: 03/15/2018

DUNS Number:

EIN Number:

Recipient Organization: University of Central Florida, 4000 Central Florida Boulevard, Orlando FL 32816

Recipient Account Number:

Grant period: 01/2014-12/2017

Reporting period end date: 12/31/2017

Signature of submitting official

Mary Davis Digitally signed by Mary Davis
Date: 2018.11.13 14:47:04 -05'00'

Purpose and objectives of the project

The goal of this proposal is to quantify the matrix effects (moisture, texture) on the LIBS elemental analysis of soil samples and correct for them for a reproducible elemental profile. This project will fulfill this goal in three steps: (i) the effect of moisture content on the LIBS signal and its reproducibility will be studied for three types of grain size (sand-, silt- and clay-type). The study will first investigate the elemental profile of major elements and then minor elements. Validation with certified NIST samples will be performed. (ii) Once the effect of moisture and temperature will be understood on "pure soils", the project will evolve towards more realistic soils. Controlled mixtures of sand-, silt- and clay-type powders will be fabricated to simulate soil textures and extend the conclusions of the first step. Validation with certified soil NIST samples will be performed. (iii) From the conclusions from the previous steps of the study, a spectral correction protocol will be established to be able to correct the LIBS emission spectra and retrieve the correct elemental signature by compensating for the eventual unknown physical state of the soil (moisture, type, grain size). This correction will be spectrum-based and include physical information from the plasma rather than uncontrolled multivariate analysis.

Project Design

To obtain reliable LIBS data from a powder such as soil, we studied different aspects of the laser-matter interaction that are involved in the laser-ablation and their influence for the analytical performance of the technique for eventual use as a screening method for soil via its elemental analysis. These parameters are:

- Wavelength of the laser to obtain a better coupling with the powder
- Effect of powder size and moisture on LIBS signal and calibration curves

We also were confronted to the presence of oxide signatures in the LIBS signal and coded an algorithm taking into account molecular formation when the analysis of oxides in air is performed.

A. MODELING OF THE SCATTERING OF THE LASER IRRADIATION WITH POWDERS

The LIBS analysis of powders starts with their irradiation by the laser. Nevertheless, in comparison with "semi-infinite" solid samples, the effect of scattering is very large on the amount of energy that is absorbed by the powders for laser ablation. This is the reason why a first set of experiments is to compare the way the laser will interact with powders of different particle size, especially by determining the scattering and absorption coefficients.

A theoretical approach to such study was laid out by Kubelka and Munk (K-M) in 1931 [Kub31] and then later in 1948 [Kub48, Kub54] to study the interaction of light with a layer of material. The K-M model is based on several assumptions:

- This is a 1D approach (finite thickness but infinite width and length)
- Perfectly diffuse and homogeneous illumination
- Only scattering and absorption are considered (no polarization, no fluorescence)
- Isotropic and homogeneous medium

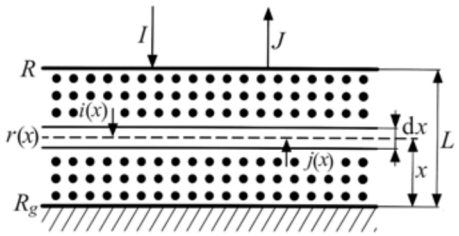

Figure 1. Light path of the Kubelka-Munk model in conjunction [Ves11]

The reflectance of the medium of thickness L is denoted R and its transmittance T. The sample is placed on top of a substance with known reflectance R_g and is split into a series of layers of equal thickness dx. Each layer receives a flux i traveling downward and a flux j traveling upward. The reflectance of that layer is then deduced as j/i.

From one layer to another, the fluxes are changed. Without scattering, just absorption is considered and as a consequence $\frac{di}{dx} = -Ki$, K being the absorption coefficient. Scattering decreases the flux downward and is considered in the K-M model to be a first order phenomenon $\frac{di}{dx} = -Ki + Sj$.

Two coupled differential equations can be derived for the downward and the upward fluxes:

$$\begin{cases} \frac{di}{dx} = -Ki - Si + Sj \\ \frac{dj}{dx} = -Kj - Sj + Si \end{cases} \quad (1)$$

If we define the transmitted value of $I=I_t$ at the bottom of the layer

$$T = \frac{I^t}{I_0} \quad (2)$$

And the reflectance factor as the ratio of the upward flux to the initial flux

$$R = \frac{I^r}{I_0} \quad (3)$$

Then the equations can be solved given the value of R_∞ for the case of an infinite layer and the known reflectance R_g of the bottom substance.

$$R = \frac{\frac{R_g - R_{oo}}{R_0} - R_{oo}\left(R_g - \frac{1}{R_0}\right) \exp\left(sL\left(\frac{1}{R_0} - R_{oo}\right)\right)}{R_g - R_{oo} - \left(R_g - \frac{1}{R_{oo}}\right) \exp\left(sL\left(\frac{1}{R_{oo}} - R_{oo}\right)\right)} \quad (4)$$

In the case of positive scattering and absorption as well as an infinitely thick sample, the reflectance of the material should be the same for two backgrounds of extreme reflectance ($R_g = 1$ and 0). This thickness is usually few layers of material. In this case, there is the relation between K and S:

$$\frac{K}{s} = \frac{(1-R_{oo})^2}{2R_{oo}} \quad (5)$$

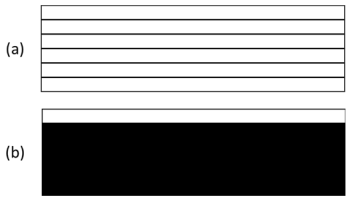

Figure 2. a) the reflectance configuration for R_{oo}, b) the reflectance configuration for R_0 (R_g=0)

In the case of R_g=0 (black background) we can deduce:

$$R = \frac{1}{L\left(\frac{1}{R_{oo}} - R_{oo}\right)} \ln\left[\frac{(1-R_0R_{oo})R_{oo}}{R_{oo}-R_0}\right]$$
$$R = R\frac{(1-R_{oo})^2}{2R_{oo}} \quad (6)$$

By comparing the amount of light absorbed by different powders, it will be possible to adapt the amount of laser power needed to produce a laser-induced plasma for LIBS with the same effective laser power.

The instrumental setup consisted in a Light source from Deuterium Lamp coupled with monochromator (Figure 3a). The beam is focused onto the sample put at the base of the integrating

sphere. The inside of the sphere is coated with Spectralon®. The integrating sphere is kept inside the aluminum foil covered box to prevent ambient light from entering the sphere (Figure 3b). The monochromator has a resolution of 5 nm. The power meter has the resolution of 1 nW.

The sample was prepared in a Teflon sample holder (Figure 3c) with black plunger with reflectivity less than 5%. Thickness of the powder is set by moving the plunger. Vernier caliper with 0.02mm resolution is used to measure the depth.

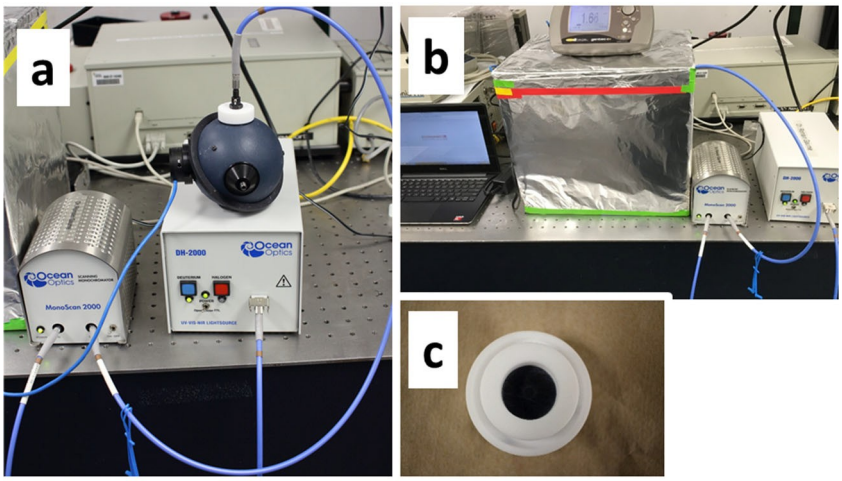

Figure 3. Experimental setup for the measurement of scattering and absorption coefficients. Details in the text.

The reflectance measurement was done from 340nm to 720 nm with 20 nm interval. Spectralon was used as reference.

For each thickness, the measurement was repeated three times. After the completion of a measurement, the holder was emptied and refilled to take into the account the variability of powder surface. The powders were levelled with a glass slide without compacting.

The thickness of the powders were gradually decreased until the reflectivity changed.

Let P_A=Power output with material A in the base, the reflectance of the powder is defined as (P_{powder}/P_{teflon}) taking Teflon as the reference.

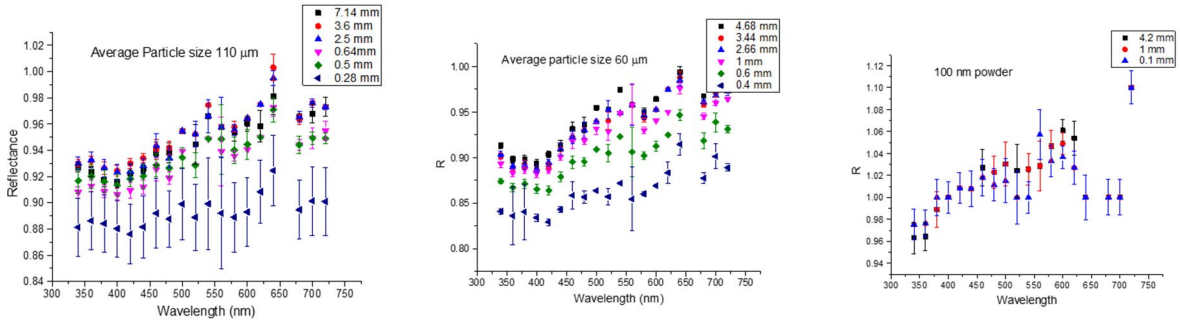

Figure 4. Reflectance measurement for particles of 110um, 60um and 110 nm

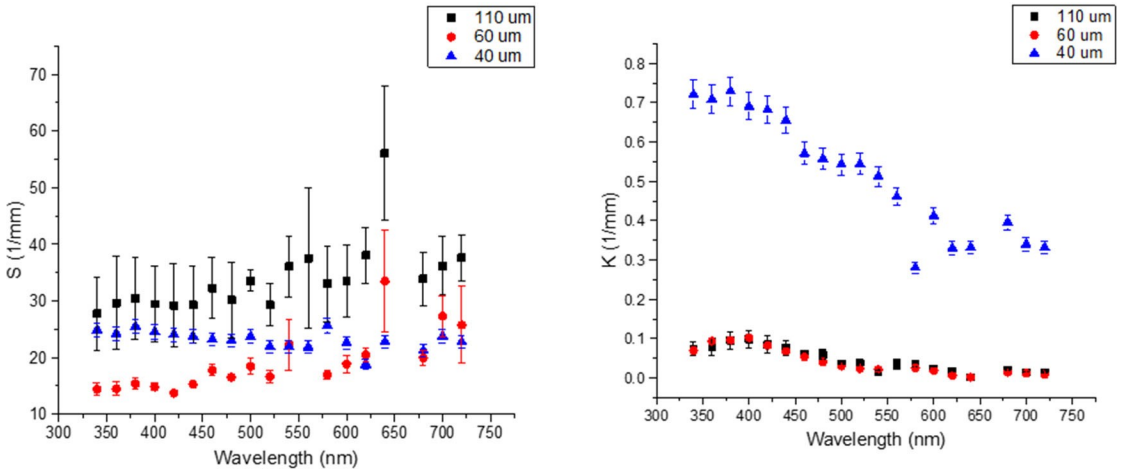

Figure 5. Scattering and absorption coefficient for powders of different diameters

These values could then be used (by extrapolation) for evaluating by modeling the heat deposition of 1064-nm radiation in the different types of media. This was done by Monte Carlo simulation. Results are shown below to compare 60 micrometer-diameter powders to 100 nm-diameter powders.

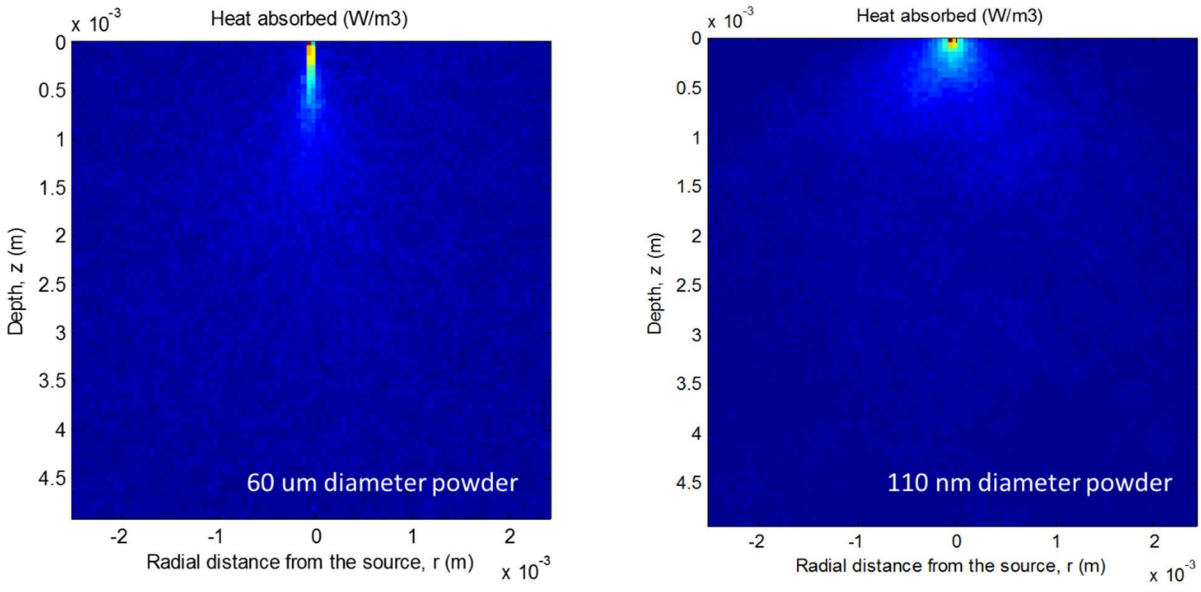

It is clearly demonstrated that the laser absorption is different for the two types of powder. The laser deposits heat deeper in the 60 μm powders than the 100 nm powders, which can affect the amount of mass that is interrogated in LIBS and as a consequence, change the plasma density and temperature and as a consequence the LIBS signal and the elemental ratio that could be deduced.

B. EFFECT OF GRAIN SIZE AND MOISTURE ON THE SIGNAL

The instrumental setup for the LIBS experiment is shown in Figure 6. First harmonics of Nd: YAG laser (1064 nm) is used for material ablation. The laser is guided by the periscope system on to the infrared reflective mirror which then directs the beam towards the focusing lens. The light from the plasma formed on the sample surface by laser irradiation is focused onto an optical fiber which transports the light to the SpectraPro® 2500i spectrometer (Action Research Corporation). The spot size of laser on the sample surface is 100 μm.

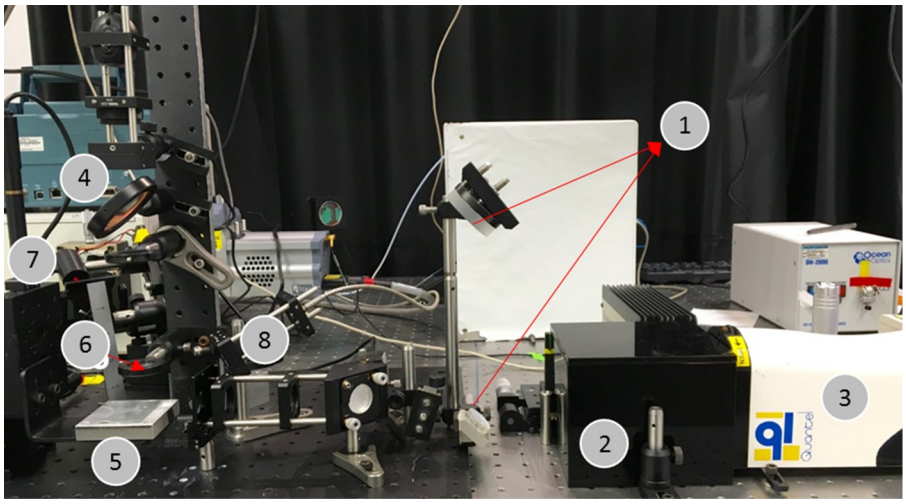

Figure 6: LIBS system. 1-Periscope system. 2-Polarizer for controlling the laser energy. 3-Nd: YAG laser (Quintel). 4-Infrared mirror. 5-Motorized sample stage. 6-Focusing lens. 7-Laser pointer for fixing laser to sample distance[1]. 8-Collection system for plasma light which is then fed into the spectrometer via optical fiber.

For the systematic study of particle size effect on LIBS spectrum, three grams of aluminum oxide powder of sizes 100 nm, 1µm and 60 µm (99.99% purity, Inframat® Advanced Material™) were dried in vacuum oven for 24 hours at 120 ℃ This is necessary to get rid of adsorbed moisture on the particle surface. The powders were then loosely packed in a 1-inch diameter and 5mm deep sample holder for laser ablation. The spectrometer delay and CCD gate width was set to 300 ns and 150 ns respectively. Single laser shot was used to collect the spectrum. The sample surface was rearranged to make it as smooth as possible and the distance between the surface and the laser focusing lens was kept at a predetermined value before firing the laser. A typical spectrum for these samples is shown in Figure 7. The signal is clean with minimal noise.

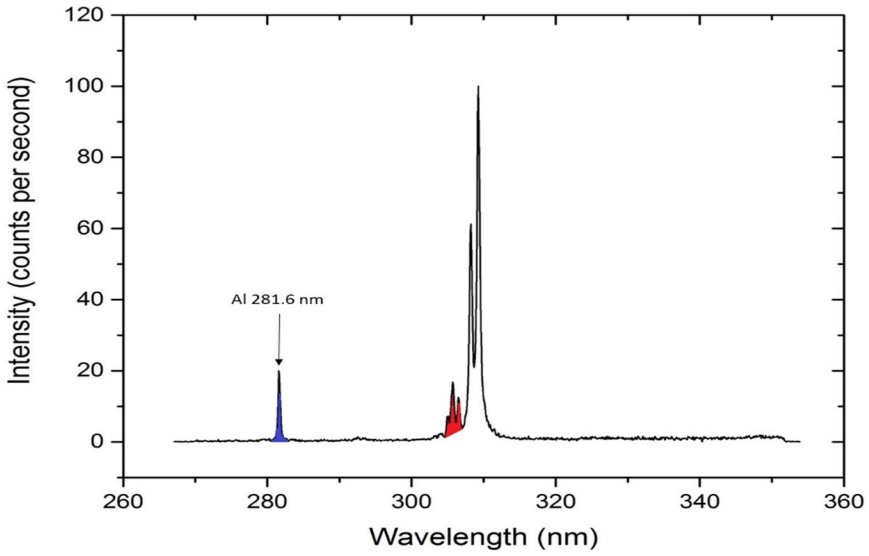

Figure 7: Typical LIBS spectrum of alumina powders.

For each particle size, variation of area under aluminum 281.6 nm peak (blue area in Figure 7) normalized by total area under aluminum 305 nm, 305.7 nm and 306.6 nm peaks (red area in Figure 7) was studied for different laser energies. The first peak belongs to Al^{+} whereas the later three belong to neutral aluminum. These peaks do not involve ground state transition and hence unlikely to be self-absorbed. The result of this experiment is shown in Figure 8.

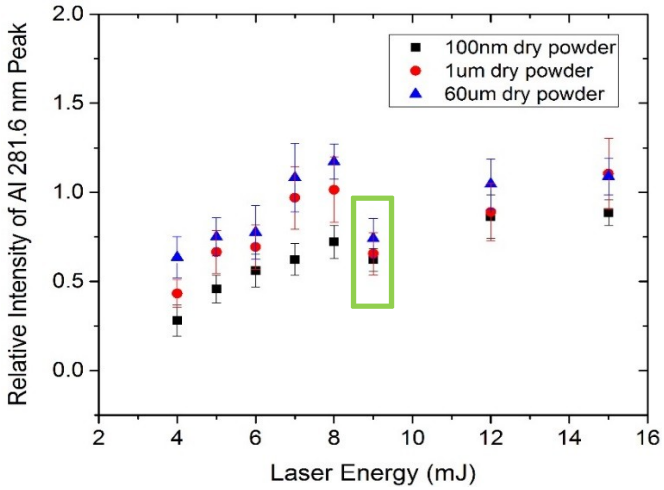

Figure 8: Relative intensity of aluminum 281.6 nm peak as a function of particle size and laser energy. The size effect is minimum at 9mJ laser energy (green box).

For a given particle size, the relative intensity increases with energy and can be understood from Saha ionization equation. For a plasma gas composed of single element, the concentration of ions in i^{th} state of ionization is given by:

$$\frac{n_e n_i}{n_{i-1}} = 2\left(\frac{2\pi m_e k_B T}{h^2}\right)^{3/2} \frac{g_i}{g_{i-1}} \exp\left[-\frac{(E_i - E_{i-1})}{k_B T}\right] \quad (7)$$

Where n_e is the electron density, n_i is the density of atoms in i^{th} ionization state, m_e is the mass of an electron, k_B is the Boltzmann's constant, h is the Plank's constant, ε_i is the ionization energy for the i^{th} ion, T is the plasma temperature and g_i is the degeneracy of the i^{th} state.

The radiant intensity of spectral line of a given species is given by:

$$I = \frac{hcn^0 gA}{4\pi\lambda Z} \exp\left(-\frac{E}{k_B T}\right) \quad (8)$$

Where n_0 is the concentration of the species, A is the transition probability, λ is the wavelength, Z is the partition function of the species and ε is the upper level of transition. The blue area in Figure 7 is contributed by singly ionized aluminum species whereas the red area is due to transition from neutral aluminum. From 1 and 2 it can be shown that for constant electron density, the relative

intensity of 281.6 peak increases with plasma temperature and hence the laser energy. The figure shows that the relative intensity also increases with particle size as predicted by Monte Carlo simulation. The slope of the curve increases up to 8 mJ for all particles and then the slope decreases abruptly. At 9 mJ the relative intensity, within the error bars, is the same for all particle sizes. *Thus by measuring relative intensity as a function of laser energy, optimal fluence can be found at which the size effect is be minimal.*

The next set of experiments investigate the influence of moisture in LIBS spectra. To this end 4,8 and 12 weight percent water was added to each powder. The powder was first put on the sample holder as in earlier experiment and set amount of water was dropped by micro-pipettor. The powder was then mixed with spatula to homogenize the moisture level. The effect of moisture in the relative intensity at various laser energies is shown in Figures 9 and 10.

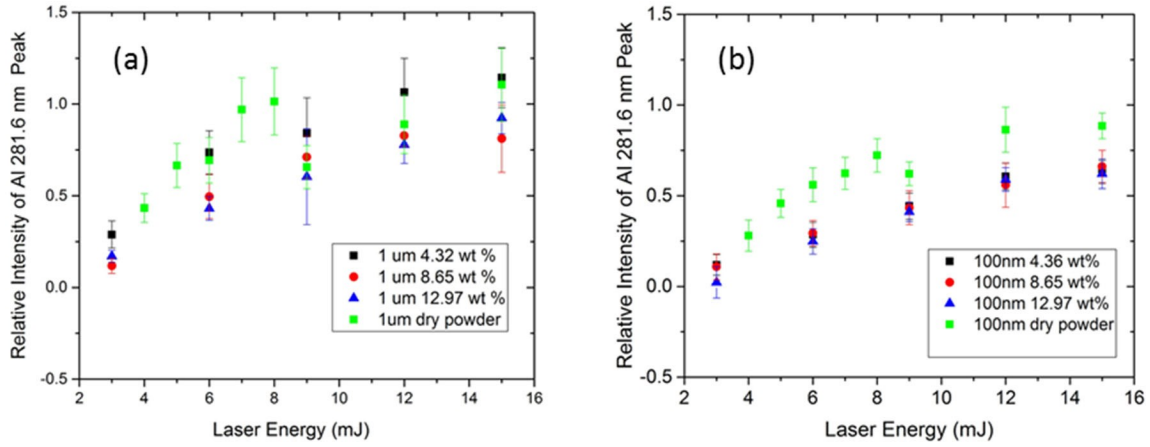

Figure 9: Effect of moisture on relative intensity of Al 281.6 nm peak. (a) 1 μm powder. (b) 100 nm powder.

In the case of 1 μm powder, relative intensity decreases with moisture content. For 100 nm powder, the moisture content, within the limits of this study, has no effect on relative intensity but the intensity is lower than that of of dry powders. It may be because of the fact that for the same

amount of water added to the powders, the layer of water adsorbed on the surface of the particles is thicker in the case of powders with smaller particle size. This hypothesis is substantiated by the observation that by adding more water, the relative intensity of 1 μm powder approaches that of 100 nm powder (Figure 10). In the case of 100 nm powder, the moisture level gets saturated even by the addition of 4.36 wt% water.

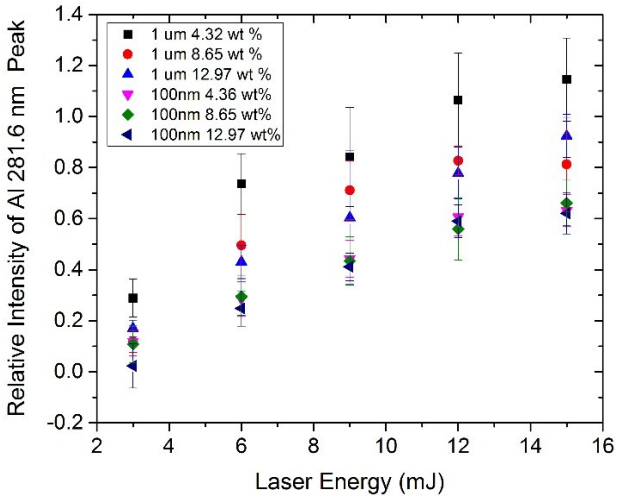

Figure 10: Comparison of moisture effect in powders of different particle sizes.

The error bars in the case of dry and wet powder are large due to inhomogeneous surface, inherent to loose powders. To minimize this effect, the powders were compacted to half an inch diameter pellet. The densities of the pellets were approximately 15 to 20% that of fully dense alumina. The result of laser energy versus relative intensity for pellets of particle size 100 nm and 1 μm are shown in Figure 11.

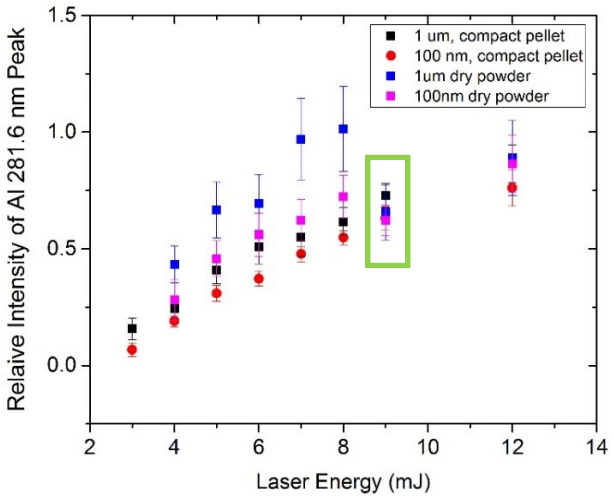

Figure 11: Comparison of relative intensity as a function of laser energy for compact powders.

The error bars have been reduced and there is no sudden change in slope as in the loose powders. The size effect is minimized as compared to loose powders and again at 9 mJ, the relative intensities are equal within the error bars. *These study suggest that working with compact powders reduces the variability of LIBS signal as well as mitigates the size effect. Moisture has a significant effect in LIBS signal and should be avoided for reliable comparison of results*.

The different varieties of α-alumina powders used in this study are labelled S1, S2 and S3. Sample S1 (99.99% purity, Inframat® Advanced Material™) is composed of 190 ± 64 nm-sized particulates agglomerated into particles with average hydrodynamic diameter of 180 nm. Sample S2 (99.99% purity, Inframat® Advanced Material™) has a similar morphology, with ultimate particle size of 500 ± 160 nm but an average hydrodynamic diameter of 1.7 µm. The hydrodynamic size distribution, measured by ultrasound spectroscopy (Acoustosizer II, Colloidal Dynamics), shows that sample S1 has very few agglomerates whereas S2 has a very broad size distribution ranging from few tenth of nanometers to hundreds of micrometers. Sample S3 (99.9%, Alfa Aesar) has an average particle size of 35 ± 13 µm. SEM images of these samples are shown in Figure 12.

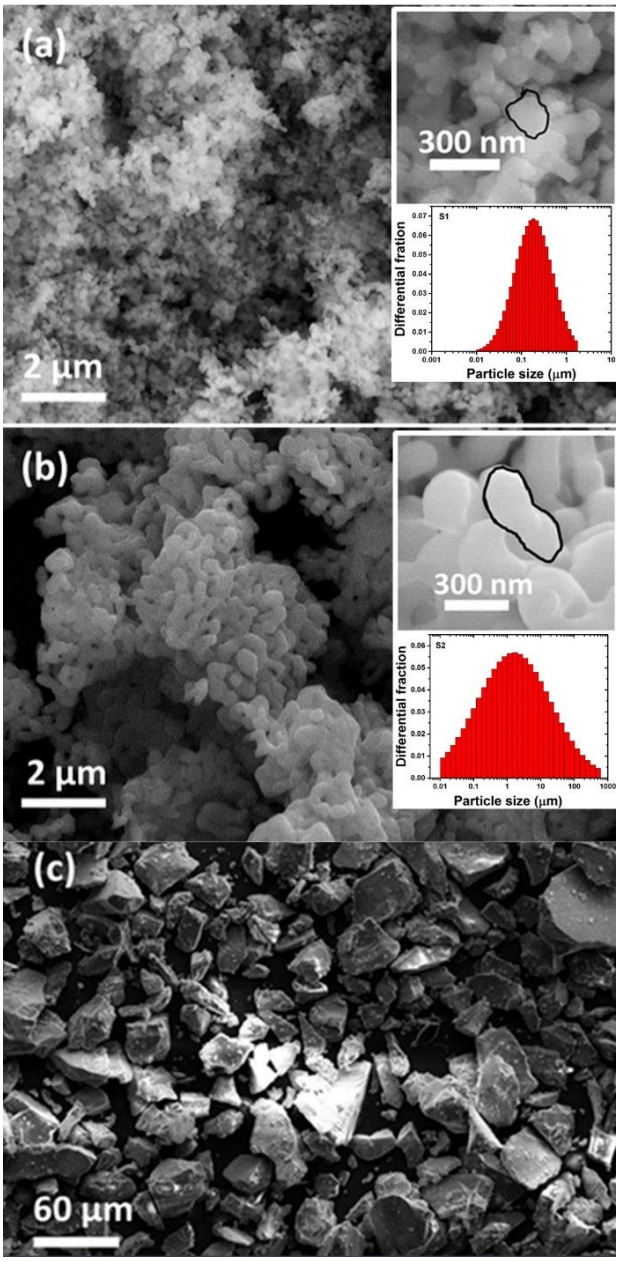

Figure 12. SEM images of alumina powders used in this study.

The inset is the image taken at higher magnification and hydrodynamic size distribution. (a) Sample S1 (b) Sample S2 (c) Sample S3.

To prepare the samples with varied nickel doping concentrations, 2.5 mg of nickel chloride hexahydrate crystallites (Scientific Products, Irvine, California) were dissolved in 250 ml of deionized water and appropriate amount of this solution was added to 3-g aliquots of alumina

powder. The mixture was homogenized in the presence of ethanol for 30 min in an alumina mortar, dried and then pressed to the desired density in a stainless-steel die. All the densities mentioned in this paper are given relative to that of fully dense alumina (3.98 g/cm3). The concentration of nickel was varied from 500 to 3000 ppm, by 500 ppm increments. The densities of S1 and S2 were varied from 13% (loose powders) to 46%, and 16% to 43%, respectively while S3 had a single density value of 41% and could not be compacted further due to the coarseness of the alumina grains.

The LIBS system was a custom-built setup. A Q-switched Nd:YAG laser (1064 nm, 5 ns, 10 Hz Quantel) was used as the ablation source. The laser light first passes through a light valve (P) for energy control and gets reflected off an infrared dichroic mirror (M) towards a converging lens L1 (2.54 cm focal length). The laser beam is focused few hundreds of micrometer below the sample surface to prevent air plasma and enhance signal stability. The laser beam spot-size on the sample surface is 100 μm. The distance between lens L1 and the sample surface is kept constant by a parallax based technique [Mot14]. A red-light emitting diode (LED) is directed on the sample surface. The reflected image is captured by CCD camera C2 and converted into a binary image by a computer. The position of the barycenter of this image (defined as the intensity weighted average location of the spot on the image) on the field of view is very sensitive to the vertical position of the sample and this fact is exploited to lock the lens-to-sample distance with an error of less than 5 μm. The error in displacement of the sample stage (ThorLabs) is 1 μm. The plasma is imaged, via lens L4, onto the CCD camera C1 (Thorlabs) to ascertain its stability. The lens L3 (focal length 5 cm) is used for focusing the plasma light into the entrance of a 300 μm diameter optical fiber feeding the spectrometer (Princeton Instrument SpectraPro 2500i, 1200 grooves/mm, 0.1 nm

wavelength resolution) coupled to an ICCD camera (Andor iStar). The spectral response calibration was carried out using a calibrated deuterium lamp (Ocean Optics, DH-2000).

LIBS on loose powders were carried out by putting them in a 2.5-cm diameter and 1-cm deep sample holder made of copper. The powders were filled up to the brim of the holder and levelled with a microscope slide without pressing. The densities of the samples were measured by dividing their mass by volume. The measurement errors were 10% for loose powders and 1% for compact pellets. Spectra were collected by the accumulation of 3 shots from 65 randomly selected spots on the sample surface. In the case of loose powders, the sample holder was emptied and refilled after taking 20 measurements to present fresh surface for ablation. The ICCD detection gate delay and width were set at 900 ns and 2 μs respectively. The laser pulse energy was measured by an energy meter (Gentec Solo2) and set at 9 mJ. The relative standard deviation of pulse energy measured over 500 pulses was 0.5%. The ICCD settings and laser energy were optimized for maximum signal-to-noise ratio.

Results and discussions

A typical LIBS spectrum of nickel-spiked alumina sample is shown in Figure 13. Calibration curves were built by normalizing the integrated intensity of the nickel peak at 301.2 nm ($3d^9(^2D)4p \leftarrow 3d^8(^3F)4s4p(^3P)$) by the sum of integrated aluminum peaks at 305.4 nm ($3s3p^2\,^4P1/2 \leftarrow 3s3p(^3P)4s\,^4P_{3/2}$) and 305.7 nm ($3s3p^{24}P_{5/2} \leftarrow 3s3p(^3P)4s\,^4P_{5/2}$). The normalization was implemented after baseline correction.

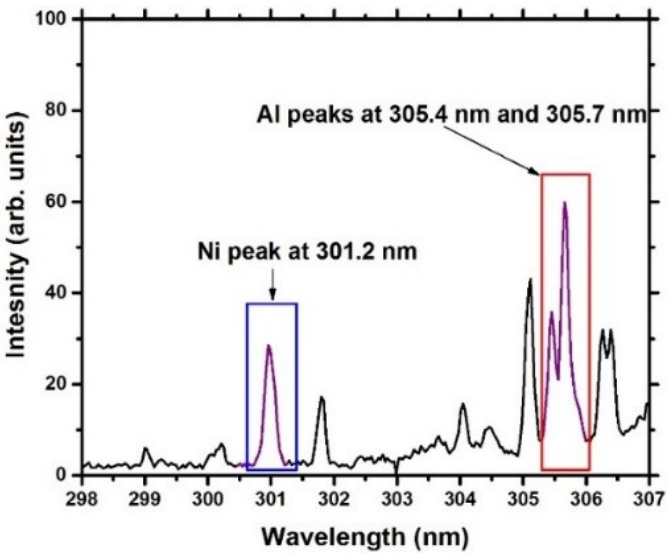

Figure 13. LIBS spectrum of nickel spiked alumina samples in between the wavelength limit 298 nm-307nm.

Figure 14 shows the comparison between the LIBS spectra of the three samples S1, S2 and S3. Each spectrum is the average of 65 spectra on sample containing 2000 ppm of nickel. The intensity of S3 is an order of magnitude larger than that of S1 powder and pressed pellet. Sample S2 shows the same features as S1. This may be due to larger scattering coefficient, governed by the ultimate particle sizes, for powders with smaller particles. In fact, Mie scattering calculations [Pra17] at 1064 nm wavelength show that 200 nm particulates scatters the incoming laser beam near-isotropically and has a scattering coefficient two orders of magnitude larger than 30 μm particles. The difference in particle shape may also have led to disparity in laser-sample coupling. Thermal conductivity, which governs nanosecond laser ablation, increases with the grain size in compact powders [Hub09], increasing the ablation rate.

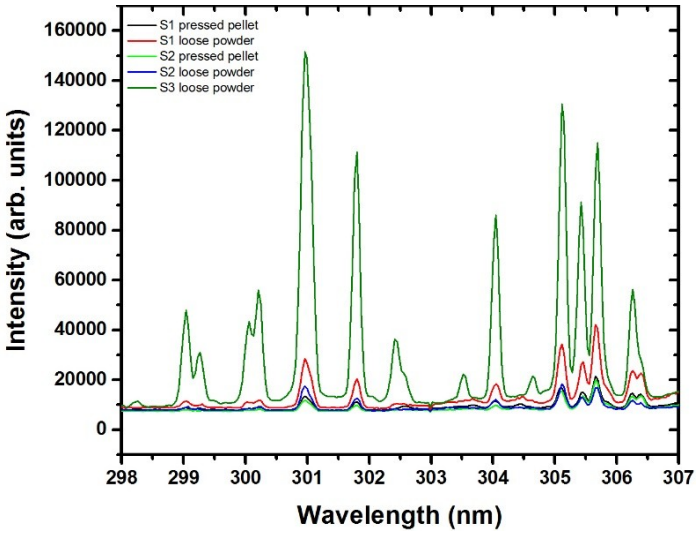

Figure 14. Comparison of spectra from S1, S2 and S3. Intensity from S3 is an order of magnitude higher than both S1 and S2 powders and pressed pellets.

It is to be noted that there are two nickel lines at 305.43 nm and 305.76 nm that can possibly interfere with aluminum lines at 305.47 nm and 305.71 nm respectively. To quantify the importance of this interference, the line intensities I_{ji} between upper and lower levels j and i of a given electronic transition, respectively, were simulated as a first approximation using the following formula [Nol12]:

$$I_{ji} = \frac{hc}{4\pi\lambda_{ji}} N^z A_{ji} \frac{g_j e^{\frac{-E_j}{k_B T}}}{U^z(T)} \tag{9}$$

Here, A_{ji} is Einstein's coefficient for spontaneous emission, N^z is the number of atoms in charge state z, g_j is the degeneracy of the sate j, E_j is the energy of the upper level, $U^z(T)$ is the partition function for the ion in charge state z at temperature T, c is the velocity of light in vacuum and h is the Planck's constant and k_B is the Boltzmann's constant. N^z was calculated using the Saha equation:

$$\frac{N_e N^{z+1}}{N^z} = \frac{2(2\pi m_e k_B T)^{3/2}}{h^3} \frac{U^{z+1}}{U^z} e^{-\frac{E_{ion}}{k_B T}} \tag{10}$$

$$\text{with } \square = \sum_0^n \square^z \tag{11}$$

where Ne is the electron number density set at $10^{18}/cm^3$ [Hah12, Nol12, Rad06], $\square_e$ is the mass of an electron, $\square_{ion}$ the ionization energy to go from charge state $\square$ to $\square+1$, and $\square$ the highest charge state of the species present in the plasma. In this simulation, the molar ratio of nickel to aluminum was set at 1.4×10^{-3}, a value equivalent to 3000 ppm of nickel by weight. The parameters for the atomic lines were retrieved from the Kurucz database [Kur95] and the atomic level data for the calculation of partition functions was retrieved from NIST atomic level database [Kra16]. The intensities as a function of temperature in the range of 5000 to 20000 K is shown in Figure 15. It can be clearly seen that at temperatures greater than 10000 K, the aluminum line intensities are more than two orders of magnitude larger than those of nickel (see inset), which justifies that, in these conditions, any interference between these two species can be neglected.

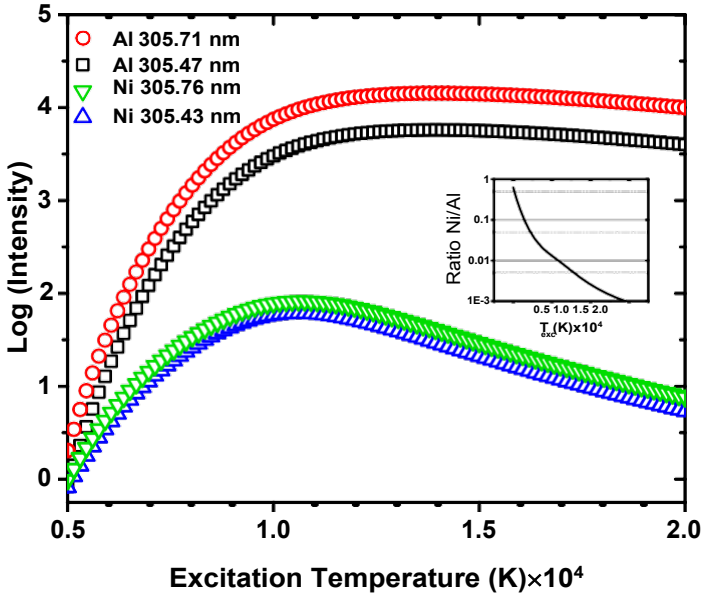

Figure 15 Simulated intensities of Al 305.47 nm, Al 305.71 nm, Ni 305.43 nm and Ni 305.76 nm peaks as a function of excitation temperature. The inset shows the ratio between the sum of Ni lines divided by the Al lines as a function of the excitation temperature.

The excitation temperature of aluminum for undoped samples was calculated for different powder compact densities using a Boltzmann plot as shown in Figure 16. The aluminum peaks at 237.21 nm, 256.79 nm, 257.51 nm and 266.04 nm were used for this purpose. The spectral data was fitted with a pseudo-Voigt function to get the integrated intensities. The excitation temperature for a given sample was calculated by averaging over 60 spectra. A comparison of all the samples shows that the regardless of the density and particle size differences, the excitation temperature remains nearly constant around a mean of 12600 K. Referring back to Figure 15, this confirms the negligible interference from nickel onto the aluminum peaks used for normalization.

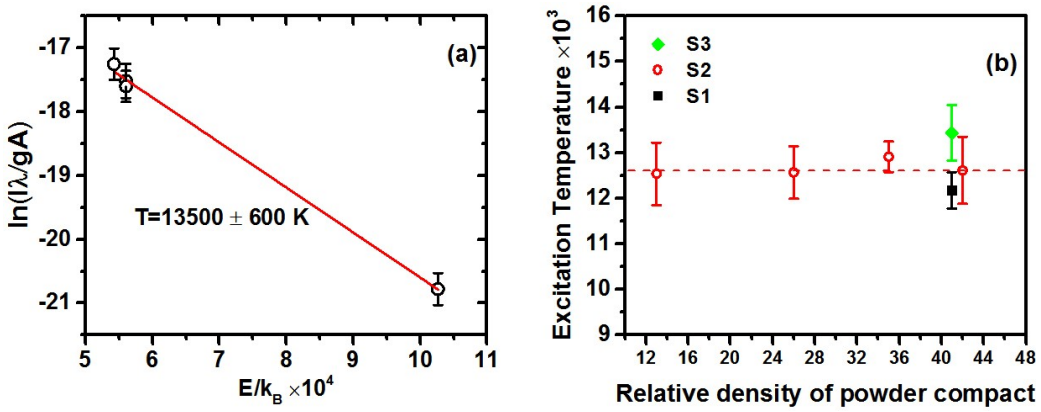

Figure 16. (a) Boltzmann plot for S3 (b) Variation of the excitation temperature of aluminum for various powder-compacts.

The calibration curves as a function of powder compaction densities for the three samples are shown in Figure 17. The shot-to-shot fluctuations in signal for samples S1 and S2 decrease significantly after compaction. The data points between 500 and 3000 ppm, which lie outside the shaded portion of Figure 17, behaves linearly. The sensitivity and its relative standard deviation (RSD) were determined from the slope of a weighed fitted line on this portion of the calibration curve and its error. Figure 18 summarizes the RSD of the sensitivity of the Ni calibration curve for

each powder and each relative density of powder compact. It can be seen that the larger the density of the powder compact, the lower the error on the calibration curve sensitivity.

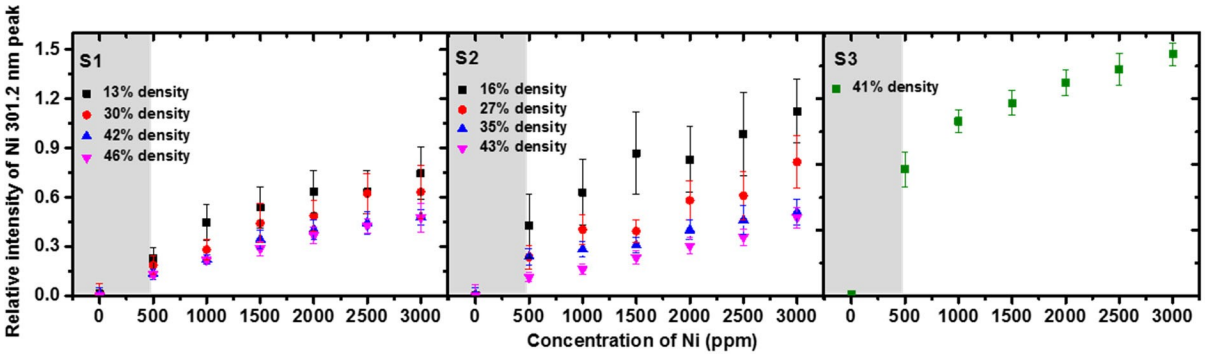

Figure 17. Calibration curve as a function of powder compaction and particle size.

The values for the sensitivity extracted from the Ni calibration curves in Figure 17 are summarized in Figure 18-left. It can be seen that for sample S1 and S2, there is no large effect of the compact density on the value of the sensitivity. However, the sensitivity seems affected by the size of the grains for a given compact density. This is visible in the case of a relative density of powder compact around 42% where the three samples could be analyzed. While the samples S1 and S2, with ultimate grain size of 190 and 500 nm respectively, show a very similar sensitivity for Ni, the value for the sample S3 (grain size of 35 μm) is increased by 90% which is statistically different from S1 and S2. This increase in sensitivity could be explained by the fact that thermal conductivity, which governs nanosecond laser ablation, increases with the grain size in compact powders [Hub09], as well as a better ablation due to the flat and sharp morphology of the grains. But more studies need to be performed to confirm the latter explanation.

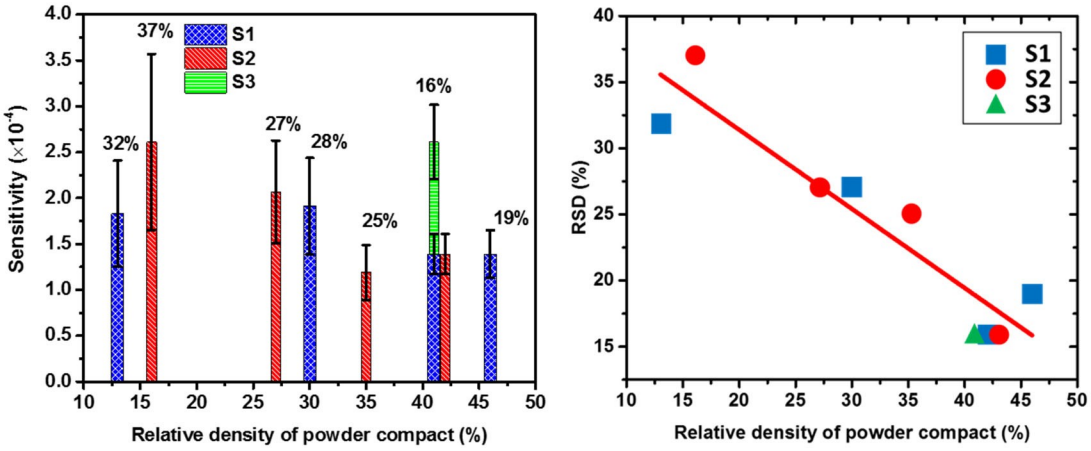

Figure 18. Effect of powder compaction on (left) the sensitivity of the Ni calibration curve (The numbers on top of the data points are the RSD values for the sensitivity) and (right) the relative standard deviation of the Ni calibration curve (the straight line is a guide to the eye to see the correlation between the two variables)

The high relative standard deviation at lower densities may be due to dissimilar shot-to-shot ablation [Siv14]. The loose powders are easy to eject, an effect which has been shown to cause intensity fluctuations in plasmas contaminated with micron-sized dust particles [Hub09, Rat07]. This effect may not be the same for each ablation event, which leads to a large fluctuation in the plasma signal, inducing a large error on the calibration curve sensitivity. All particle sizes have the same relative standard deviation for similar relative densities (Figure 18-right). For a given density of the powder compact contained in a given volume (as our study was conducted), the remaining volume between grains is the same, indifferently of the grain size. The powder compact will just be composed of less grains as the grain size increases, but the volume of material will be the same. The thermal conductivity of materials is larger when their porosity is smaller [Hub09]. Furthermore, the heat is dissipated in the randomly distributed voids in the looser powders while

the sample get more organized for smaller porosity, leading to a more homogeneous distribution of the heat than the loose powder. This may lead to a more reproducible ablation for the more compact samples

C. MODELING OF LIBS PLASMA COMPOSITION

As mentioned in previous reports, a calibration curve is needed to find the stoichiometry shift in materials. In our study, we used Yttria-Alumina mixtures (labeled YAG mixtures in the following of the report). To this end, the intensity ratio of aluminum and yttrium lines are plotted against their molar ratio as shown in Figure 19

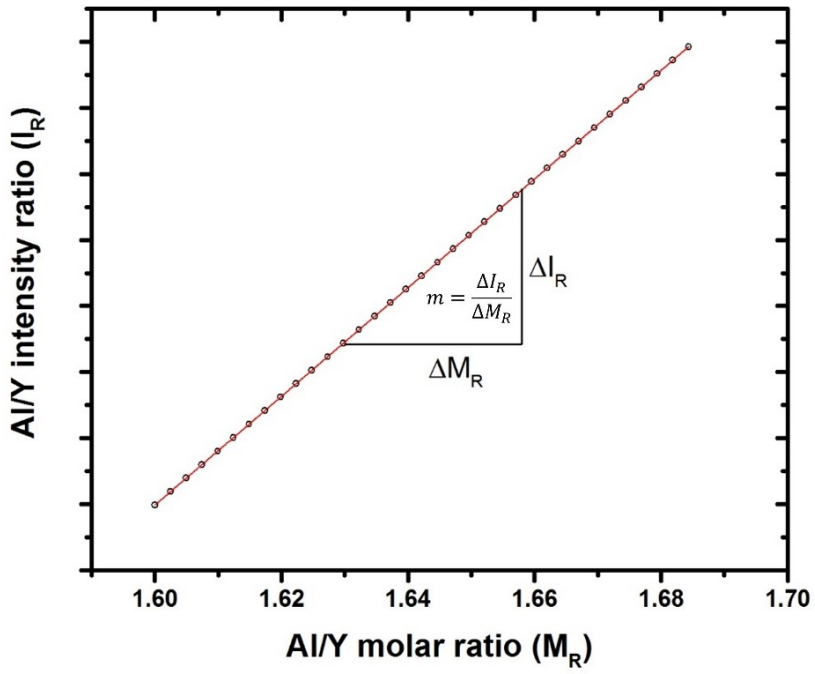

Figure 19. Hypothetical calibration curve to find the Al/Y molar ratio in YAG samples.

If the slope and intercept of the calibration curve is *m* and *c* respectively, the molar ratio of test sample is calculated by applying the following formula:

$$M_R = \frac{I_R - c}{m} \tag{12}$$

Here M_R and I_R are the molar and intensity ratios respectively.

If the standard deviation of intensity ratio is σ_{I_R}, the error in the corresponding molar ratio is:

$$\sigma_{M_R} = \frac{I_{R\text{-}c}}{m}\sqrt{\left[\frac{C_{I_{R\text{-}c}}}{I_{R\text{-}c}}\right]^2 + \left[\frac{C_m}{m}\right]^2} \tag{13}$$

Assuming that the relative errors in m and c are small compared to the relative error in I_R, equation (13) can be written as:

$$\sigma_{M_R} = \frac{C_{I_R}}{m} \tag{14}$$

To differentiate the molar ratios between two adjacent points in the x-axis of Figure 19 with 99% confidence, $3\sigma_{M_R} < \frac{1}{2}\Delta\sigma_R$ where ΔM_R is the smallest of the difference in molar ratios between adjacent samples. This implies that:

$$\sigma > \frac{6C_{I_R}}{ilM_R} \tag{15}$$

This expression shows that large sensitivity of the calibration curve is essential to accurately discern the molar ratios in YAG samples.

The ratio of emission line intensities depends on plasma temperature but how this ratio varies with it is not obvious. The change in sensitivity of the calibration curve with temperature cannot be foreseen either. The purpose of this chapter is to simulate the calibration curve at different plasma temperatures. The result of this calculation will help to obtain proper experimental protocol leading to the best sensitivity.

Calculations

Since the intensities of the emission lines at a given temperature depend on number densities of the emitters, the concentration of different atomic and molecular species as a function of temperature needs to be computed first. The plasma consists of ablated material vapor blended

with the background gas. Let n_{vap} and n_{gas} be the atomic number densities of the ablated element (A) and the background gas (B) respectively. These elements exists as atoms (A^0, A^+, A^{++}, A^{+++}, B^0, B^+,B^{++},B^{+++}), homonuclear molecules (A_2, B_2, A_2^+,B_2^+) and heteronuclear molecules (AB, AB^+). At temperatures above 3000K, formation of polyatomic molecules can be neglected [Sim72, Coc97] so that:

$$n_{vap} = n_A + \sum_{z=0}^{1} n_{AB}^z \tag{16}$$

$$n_{gas} = n_B + \sum_{z=0}^{1} n_{AB}^z \tag{17}$$

Where n_A and n_B are the number densities of element A and B excluding the molecule AB and equal to:

$$n_X = \sum_{z=0}^{3} n_X^z + \sum_{z=0}^{1} n_{X_2}^z \quad , X = A, B \tag{18}$$

Ionization states up to +3 is considered for atoms and +1 for molecules.

Assuming a plasma in local thermodynamic equilibrium (LTE), the number densities of ionic species can be obtained using Saha equation combined with conservation of mass. It is to be noted, however, that the ionization energies are lowered in plasma due to microfield and the reduction can be well approximated using Unsöld's formula[Ols61]:

$$\Delta E_z^{ion} = 3e^2 (z+1)^{3/2} \left(\frac{4n}{3} n_e\right)^{1/3} \tag{19}$$

Number density of neutral molecules is calculated using the law of mass action for chemical equilibrium [Zel65]:

$$\frac{n_A^O n_B^O}{n_{AB}^O} = \left(\frac{2nk_BT}{h^2} \frac{m_A m_B}{m_{AB}}\right)^{3/2} \frac{U_A^O U_B^O}{U_{AB}^O} e^{-\frac{E_D}{k_BT}} \tag{20}$$

Here U_{AB}^O is the partition function of a neutral molecule, E_D the molecular dissociation energy and m_A the mass of element A. The partition function of atomic species is given by:

$$U_A^z = \sum_j g_j e^{\frac{-E_j}{k_BT}} \tag{21}$$

Here, g_j is the degeneracy of energy level E_j. The atomic energy levels and their degeneracies can be found in NIST atomic level database [Kra16]. Molecular partition function is calculated using the following expression:

$$\sum_{e,-8,J} \square\square^{-P(E_e+E^{e}_{\square}+E^{e,\square}_{I})} \tag{22}$$

Here e, ϑ, and J are the electronic level, vibration quantum number and rotational quantum number respectively. The E's are the corresponding energies. The vibrational and rotational energies are given by:

$$\square^{e}_{-8} = \hbar\square\square^{e}(\square),\ \square^{e}(\square)= \square_e\left(\square+\frac{1}{2}\right) - \square_e\square_e\left(\square+\frac{1}{2}\right)^2 + \square_e\square_e\left(\square+\frac{1}{2}\right)^3 \tag{23}$$

$$\square^{e}_{J} = \hbar\square\square^{-8}_{J}(\square),\ \square^{-8}_{J}(\square)=\square_{-8}\square(\square+1) - \square_{-8}\square^{2}(\square+1)^{2} \tag{24}$$

With $\square_{-8} = \square_e - \square_e\left(\square+\frac{1}{2}\right) + \square_e\left(\square+\frac{1}{2}\right)^2$ and $\square_{-8} = \square_e - ß_e\left(\square+\frac{1}{2}\right)$

The second and third order terms in equations (23) and (24) arise because of anharmonic oscillations and deformable bonds. Values of the constants $\square_e$, $\square_e\square_e$, $\square_e\square_e$, $\square_e$, $\square_e$, $\square_e$, $\square_e$ and $ß_e$ can be found in NIST chemistry web book [Lin10].

The composition of LIBS plasma at a particular temperature can be calculated using a published [Her02] and outlined in Figure 20.

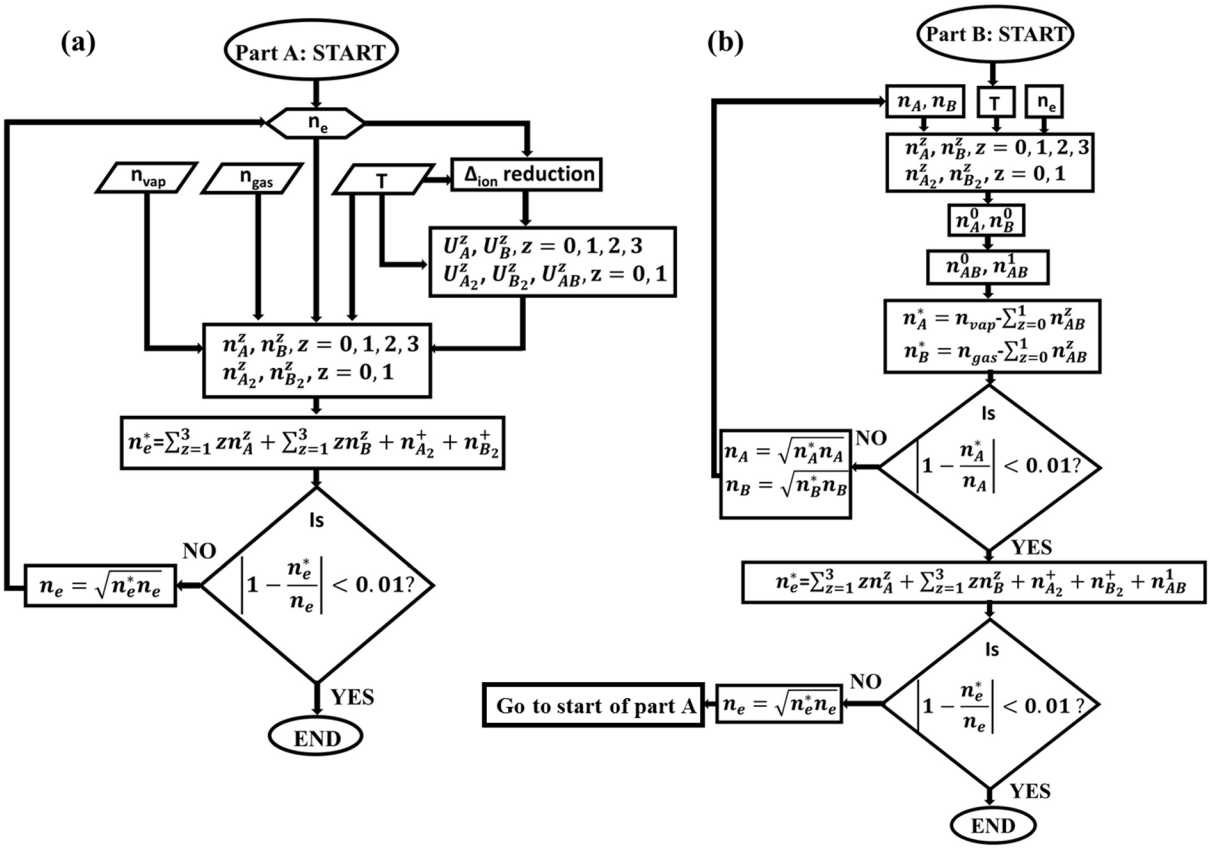

Figure 20. Algorithm flowchart for calculating number densities of different species in a plasma at local thermodynamic equilibrium. (a) Iteration loop to calculate ionization equilibrium and (b) chemical equilibrium.

The simulation is carried out using two iteration loops. The first loop is initialized with a certain electron number density n_e. Reduction in ionization potential is calculated based on equation 19 and then the partition functions are computed. Using these values, the number densities of neutral and charged atoms and homonuclear molecules are calculated. In the first part of the simulation, the material vapor and the background gas are not allowed to react so that $n_{vap} = n_A$ and $n_{gas} = n_B$. The electron density is given by:

$$n_e^* = \sum_{z=1}^{3} z n_A^z + \sum_{z=1}^{3} z n_B^z + n_{A_2}^+ + n_{B_2}^+ \quad (25)$$

If n_e^* and n_e differ by more than a percent, the value of n_e is updated as shown in Figure 20 (a) and the calculation is repeated. After this loop converges, second iteration is initiated in which neutral species of elements A and B are allowed to react to form neutral AB. After computing the values of n_{AB}^0 and n_{AB}^+, the total number density of unreacted A and B are updated using equation 25:

$$n_A^* = n_{vap} - \sum_{z=0}^{1} n_{AB}^z \tag{26}$$

$$n_B^* = n_{gas} - \sum_{z=0}^{1} n_{AB}^z \tag{27}$$

Just as in charge equilibrium loop, if n_A^* and n_A differ by more than a percent, value of n_A is updated as shown in Figure 20(b) and the iteration is restarted. After convergence, the electron number density is calculated again with the addition of the electrons coming from AB^+ species:

$$n_e^* = \sum_{z=1}^{3} z n_A^z + \sum_{z=1}^{3} z n_B^z + n_{A_2}^+ + n_{B_2}^+ + n_{AB}^+ \tag{28}$$

Again, if the charge densities n_e^* and n_e differ by more than a percent, n_e is updated as before and the computation is started right from the beginning of the first loop else the computation is stopped and the number densities are returned.

Results and discussion

The code for the simulation was written in MATLAB and to test the validity of the procedure, an attempt was made to replicate the results of Hermann *et al.* [Her02]. The first trial was to simulate aluminum plasma in oxygen background. The starting values of n_{vap},and n_{gas} was set just as in the reference, i.e. 1×10^{22} m^{-3} and 1.1×10^{22} m^{-3} respectively. The result in the temperature range 4000 to 12000 K is shown in Figure 21 and shows that our results (solid lines) are in excellent agreement with the results from the reference (circles). The results for aluminum plasma in nitrogen, also a replication of the simulation from the same reference, is shown in Figure 22 which further substantiates our procedure.

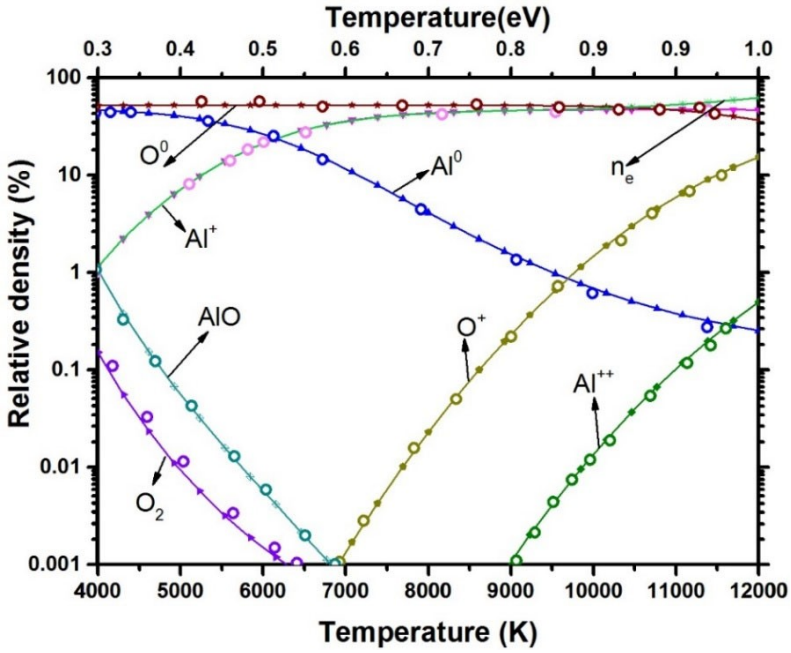

Figure 21 Number densities of plasma species as a function of temperature computed for aluminum. Circles are the simulation by Hermann et al [Her02] and the solid lines are our result. The number density of each species was normalized by the sum n_{vap} + n_{gas}.

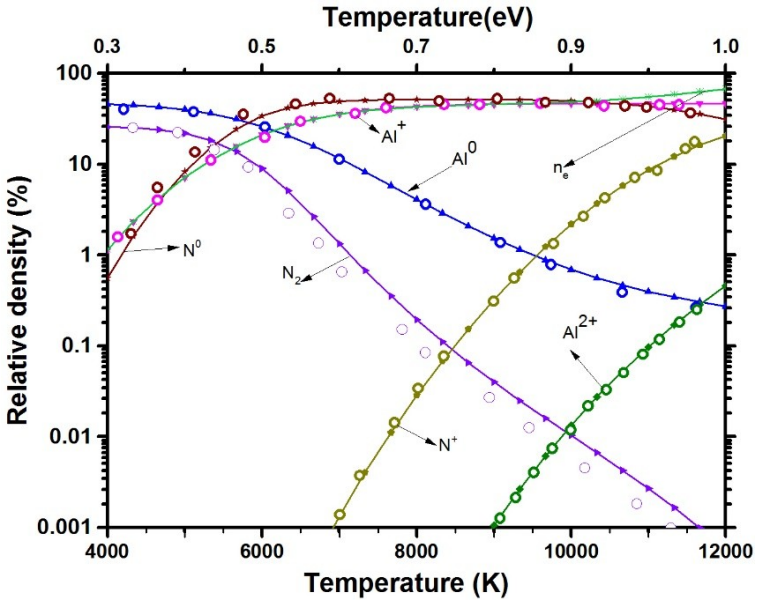

Figure 22 Simulation of aluminum plasma in nitrogen background. Circles are the results from Hermann et al. [Her02] and the solid lines are our result.

The slight discrepancy in the number densities of nitrogen molecules in Figure 22 may be due to omission of Λ-type doubling factor and nuclear statistical weight. Apart from this small difference, atomic number densities, which dictate the emission spectrum of LIBS plasma, are in very good agreement.

After the validation of the simulation code, composition of YAG plasma in air was determined using the same algorithm. The number of moles of YAG ablated from the sample was calculated based on the experimentally observed crater size. The diameter of the crater on the surface of YAG samples is 100 μm. Assuming that all the ablated mass from the 100 μm diameter hemispheric crater goes into the plasma, the number density of YAG formula units ($Y_3Al_5O_{12}$) in the plasma will be 1.71×10^{23} m^{-3}. This corresponds to $5\times1.71\times10^{23}$ aluminum atoms, $3\times1.71\times10^{23}$ yttrium atoms and $12\times1.71\times10^{23}$ oxygen atoms per meter cube. Plasma diameter of 3 mm was assumed based on which the number density of oxygen and nitrogen atoms contributed by air enclosed in a sphere of 3 mm diameter was calculated. Setting the pressure to 1 atm, temperature to 300 K and nitrogen to oxygen ratio to 3.7, ideal gas law was applied to this sphere resulting in 1.08×10^{25} m^{-3} oxygen atoms and 3.8×10^{25} m^{-3} nitrogen atoms. Electron density of 1.5×10^{23} was taken to initialize the simulation. The variation of number densities of different species in the temperature range 5500 K to 18000 K is shown in Figure 23.

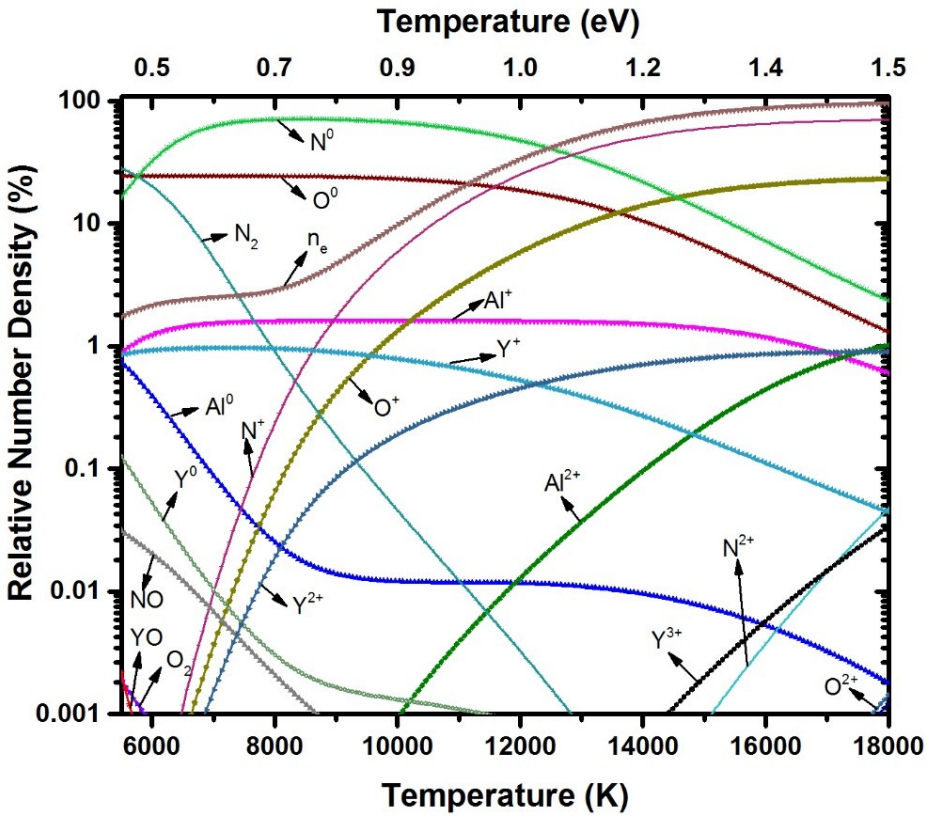

Figure 23. Simulation of YAG plasma in air. The number density of ablated YAG molecules was estimated to be 1.71×10^{23} m^{-3} based on the experimentally observed crater size. The air pressure was set to 1.01×10^{5} Pa and the ratio of nitrogen to oxygen atoms was set to 3.7 to simulate the atmospheric condition.

From Figure 23, it can be inferred that above 10000 K, electron number density follows the trend of N^+. The neutral atomic species Y^0 and Al^0 varies rapidly with temperature up to 8000 K. Al^0 levels off after this temperature while Y^0 becomes vanishingly small. On the contrary, the singly charged species Al^+ and Y^+ are relatively stable with temperature. This trend suggests that emission lines from Al^+ and Y^+ should be chosen for analysis so that shot-to-shot fluctuation in plasma temperature will have minimal influence on the intensity ratio. Because of the close

proximity of the upper energy levels, Al 281.61 nm and Y 278.52 nm lines were chosen to see the behavior of Al/Y intensity ratio with temperature (Figure 24).

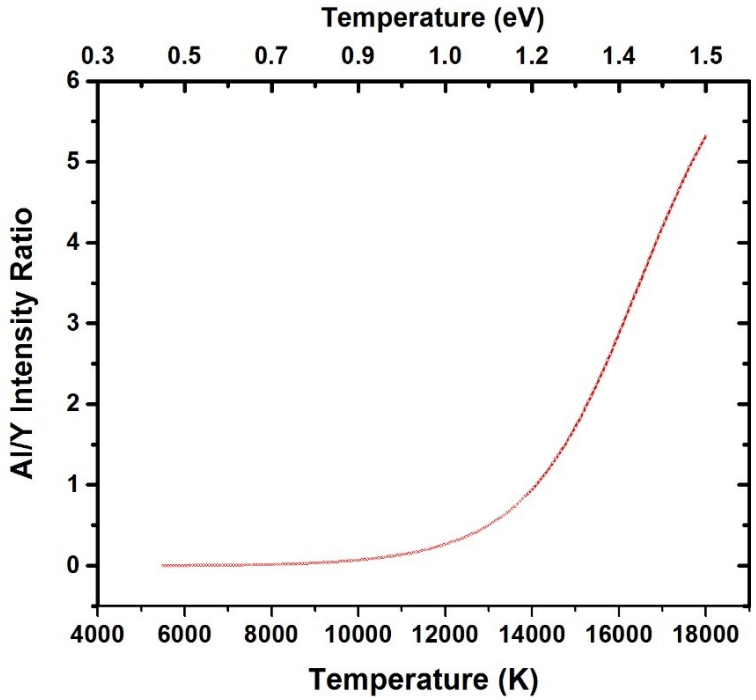

Figure 24. Simulated Al/Y intensity ratio as function of plasma temperature. Al 281.61 nm and Y 278.52 nm peaks were used for this purpose.

The intensities were calculated using equation (9) and the values of A_{ji} , g_j and λ_{ji} were extracted from Kurucz database[1] The ratio increases sharply after 12000 K which suggests that above this temperature, a tiny fluctuation in plasma temperature can produce large variation in the intensity ratio. However, this does not elucidate how the behavior of sensitivity with temperature.

[1] Kurucz, R.L. *The Kurucz Smithsonian atomic and molecular database*. in *Astrophysical Applications of Powerful New Databases*. 1995.

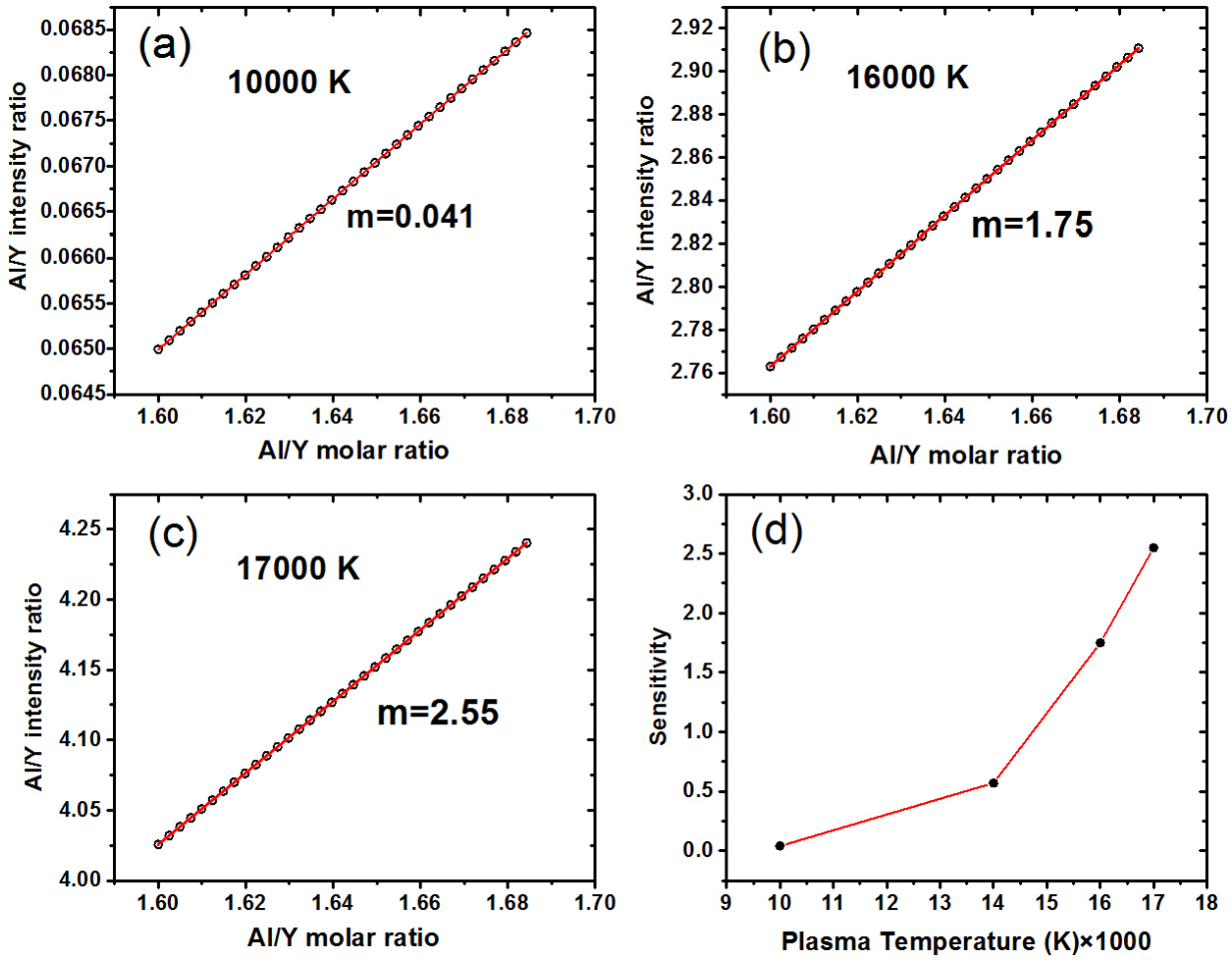

Figure 25. Sensitivity of the simulated calibration curve. The results show that the sensitivity increases sharply after 14000 K.

To this end, a simulation was performed in four different temperatures and at each temperature the molar ratio of Al/Y was varied from 1.6 to 1.68 with a step size of 0.0025 (Figure 25). The results show that the sensitivity rapidly increases above 14000 K. Though the results from Figure 24 suggest that effect of shot-to-shot temperature fluctuation is lower below 10000 K, the molar ratios are too small to resolve experimentally.

Implications for Criminal Justice Policy and Practice in the U.S.

The results of this study show the importance of considering sample preparation when LIBS is used for the analysis of powders. Two main factors (particle size and moisture) have been studied and show that the potential field examiner using LIBS, moisture needs to be eliminated and high compaction needs to be used for the creation of pellets in order to obtain reproducible data and being able to compare calibration samples and field samples, even as complex as soil. In summary, LIBS in the field for soil analysis using a general protocol is not recommended and for quantitative decision making, even screening, the dehydration of samples in a particulate form and their compaction into a pellet with high density are necessary.

Scholarly products

PUBLICATIONS

1. Sudeep Jung Pandey, Richard Locke, Romain Gaume, Matthieu Baudelet, "Effect of powder compact density on the LIBS analysis of Ni impurities in alumina powders", Spectrochimica Acta Part B: Atomic Spectroscopy, Volume **148**, 99-104 (2018)
2. Sudeep Jung Pandey, Mauro Martinez, Jan Hostaša, Laura Esposito, Matthieu Baudelet and Romain Gaume, "Quantification of SiO2 Sintering Additive in YAG Transparent Ceramics by Laser-Induced Breakdown Spectroscopy (LIBS)", Optical Materials Express, **7**(5), 1666-1671 (2017)
3. S.J. Pandey, M. Martinez, F. Pelascini, V. Motto-Ros, M. Baudelet, R.M. Gaume. "Quantification of non-stoichiometry in YAG ceramics using laser-induced breakdown

spectroscopy", Optical Materials Express, **7**(2), 627-632 (2017)

PRESENTATIONS

1. Sudeep Jung Pandey, Richard Locke, Mauro Martinez, Romain Gaume, Matthieu Baudelet, "Study of Matrix Effects for Reproducible LIBS Analysis of Powders", SciX 2016; Minneapolis, MN, USA; 12/19, 2016. *Invited*

2. Sudeep Jung Pandey, Richard Locke, Brandon Seesahai, Romain Gaume, Martin Richardson, Matthieu Baudelet, "Study of Matrix effects for reproducible LIBS analysis of powders", Pittcon 2016; Atlanta, GA, USA; 03/08, 2016

3. Matthieu Baudelet, "From the calibration curve to machine learning: the evolution of quantitative LIBS data analysis", SciX 2015; Providence, RI, USA; 10/01, 2015. *Invited paper.*

4. Romain Gaume, R. Locke, M. Chun, M. Baudelet, "Towards Highly-Sensitive Stoichiometric Analysis by Laser-Induced Breakdown Spectroscopy (LIBS)"; 10th Laser Ceramics Symposium; Wroclaw, Poland; 12/04,2014; *Invited presentation*

REFERENCES

[Coc97] Coccia, L.G., G.C. Tyrrell, and I.W. Boyd, Gas-phase reactions during reactive laser ablation of Ti and Si in N2 and O2 rarefied atmospheres analysed using energy-dispersive mass spectrometry. Applied Surface Science, 1997. 109-110: p. 413-418.

[Hah12] D.W. Hahn, N. Omenetto, Laser-induced breakdown spectroscopy (LIBS), part II: review of instrumental and methodological approaches to material analysis and applications to different fields, Applied spectroscopy, 66 (2012) 347-419.

[Her02] Hermann, J. and C. Dutouquet, Local thermal equilibrium plasma modeling for analyses of gas-phase reactions during reactive-laser ablation. Journal of applied physics, 2002. 91(12): p. 10188-10193.

[Hub09] S. Hübner, A. Melzer, Dust-induced modulation of the atomic emission in a dusty argon discharge, Physical review letters, 102 (2009) 215001.

[Kra16] A. Kramida, Ralchenko, Yu., Reader, J. and NIST ASD Team NIST Atomic Spectra Database, http://physics.nist.gov/asd, in, 2016.

[Kub31] Kubelka, P.; Munk, F. Ein Beitrag zur Optik der Farbanstriche, Z.Tech. Phys. (Leipzig), 12(1931), 593–601

[Kub48] P. Kubelka, New contributions to the optics intensely light scattering materials. Part I, J. Opt. Soc. Am. 38(1948), 448–457.

[Kub54] Kubelka, P. New contributions to the optics intensely light scattering materials. Part II: Nonhomogeneous layers., J. Opt. Soc.Am. 44(1954), 330–335.

[Kur95] R.L. Kurucz, The Kurucz Smithsonian atomic and molecular database, in: Astrophysical Applications of Powerful New Databases, 1995, pp. 205.

[Lin10] Linstrom, P. and W. Mallard, NIST chemistry webbook, NIST standard reference database number 69, National Institute of Standards and Technology, Gaithersburg MD, 20899. 2010.

[Mot14] V. Motto-Ros, E. Negre, F. Pelascini, G. Panczer, J. Yu, Precise alignment of the collection fiber assisted by real-time plasma imaging in laser-induced breakdown spectroscopy, Spectrochimica Acta Part B: Atomic Spectroscopy, 92 (2014) 60-69.

[Nol12] R. Noll, Laser-induced breakdown spectroscopy, Springer, 2012.

[Ols61] Olsen, H.N., Partition Function Cutoff and Lowering of the Ionization Potential in an Argon Plasma. Physical Review, 1961. 124(6): p. 1703-1708.

[Pra17] S. Prahl, Mie Scattering Calculator, http://omlc.org/calc/mie_calc.html, in, 2017.

[Rad06] L.J. Radziemski, D.A. Cremers, Handbook of Laser Induced Breakdown Spectroscopy, in, John Wiley & Sons, West Sussex, England, 2006.

[Rat07] S. Ratynskaia, M. De Angeli, U. De Angelis, C. Marmolino, G. Capobianco, M. Lontano, E. Lazzaro, G. Morfill, G. Gervasini, Observation of the effects of dust particles on plasma fluctuation spectra, Physical review letters, 99 (2007) 075002.

[Siv14] P. Sivakumar, L. Taleh, Y. Markushin, N. Melikechi, Packing density effects on the fluctuations of the emission lines in laser-induced breakdown spectroscopy, Spectrochimica Acta Part B: Atomic Spectroscopy, 92 (2014) 84-89.

[Sim72] Simmons, J.D. and J.K. McDonald, The emission spectrum of AlN. Journal of Molecular Spectroscopy, 1972. 41(3): p. 584-594

[Ves11] Vesna Džimbeg-Malčić, Željka Barbarić-Mikočević, Katarina Itrić, "Kubelka-Munk theory in describing optical properties of paper (i)", Technical Gazette 18, 1(2011), 117-124

[Zel65] Zeldovich, Y.B. and Y.P. Raizer, Physics of shock waves and high-temperature hydrodynamic phenomena. 1965, FOREIGN TECHNOLOGY DIV WRIGHT-PATTERSON AFB OH